Supplementary Materials for

Generation of supertoroidal pulses with controlled topologies

Ren Wang[1,2*], Jinshan Cui[1], Zeyi Zhang[1], Yanhe Lyu[3], Junjie Shao[1*], Moran Zhang[1], Sheng Liu[1], Zixi Qiu[1], Bing-Zhong Wang[1], Mu-Sheng Liang[1*], Yijie Shen[3,4*]

[1] *Institute of Applied Physics, University of Electronic Science and Technology of China, Chengdu 611731, China*

[2] *Yangtze Delta Region Institute (Huzhou), University of Electronic Science and Technology of China, Huzhou 313098, China*

[3] *Centre for Disruptive Photonic Technologies, School of Physical and Mathematical Sciences, Nanyang Technological University, Singapore 637371, Singapore*

[4] *School of Electrical and Electronic Engineering, Nanyang Technological University, Singapore 639798, Singapore*

* E-mail: rwang@uestc.edu.cn (R.W.); msliang@uestc.edu.cn (M.S.L.); 909703671@qq.com (J.S.); yijie.shen@ntu.edu.sg (Y.S.)

This PDF file includes:

Supplementary Text

Figs. S1 to S24

Supplementary text and figures

1. Space–time fields and singularities of supertoroidal pulses (STPs).

The α-type STPs exhibit fractal field distributions, as shown in Fig. S1. On the spatiotemporal (ρ–t) cross-section, the zero contours exhibit a hyperbola-like shape, and their number within the field of view increases as α increases. On the longitudinal spatial (ρ–z) cross-section, the zero contours resemble "8" patterns; with increasing α, more contours appear in the field of view, forming multiple nested structures reminiscent of Russian dolls. Overall, the field distribution exhibits a fractal-like structure.

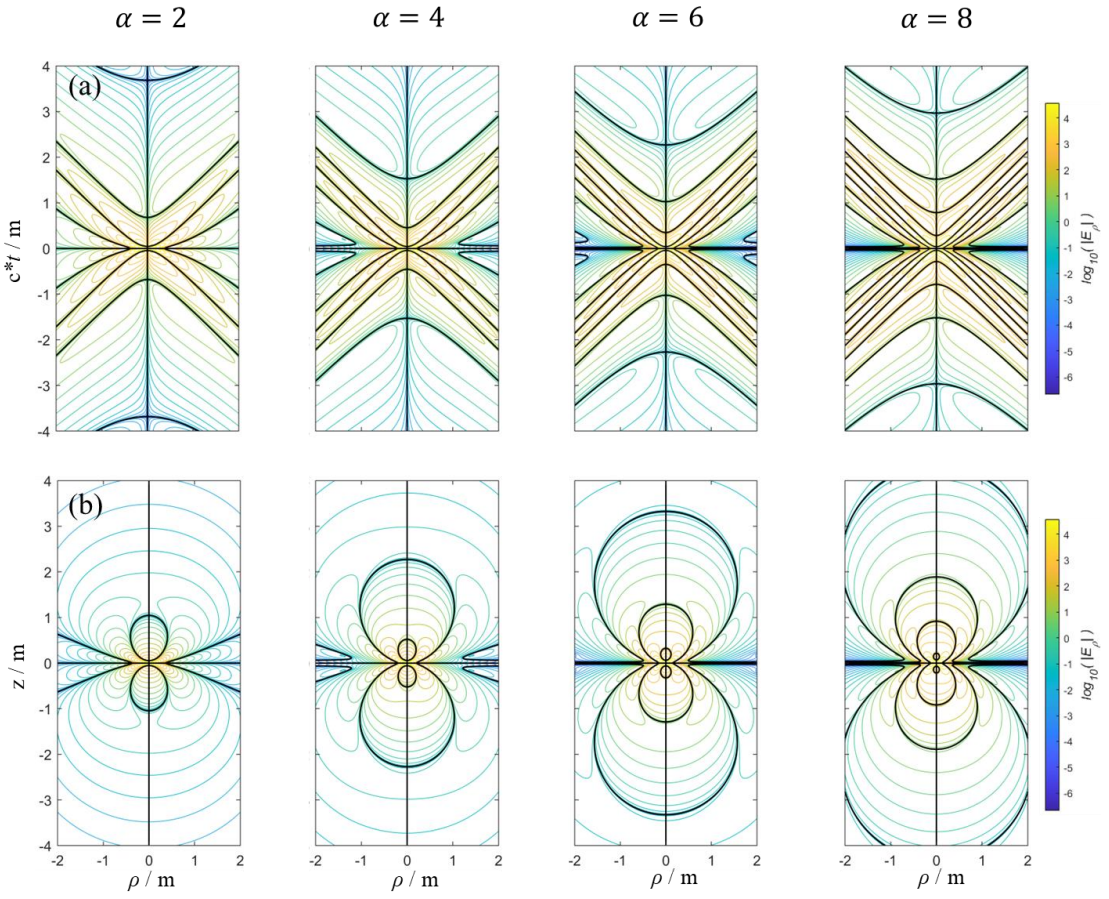


Fig. S1. Fractal field distributions of α-type STPs: (a) in the z=0 plane and (b) at

***t*=0.** The black curves represent the zero contours of the transverse polarization components. On the spatiotemporal (ρ–t) cross-section, the zero contours exhibit a hyperbola-like shape, and their number within the field of view increases as α increases. On the longitudinal spatial (ρ–z) cross-section, the zero contours resemble "8" patterns; with increasing α, more contours appear in the field of view, forming multiple nested structures reminiscent of Russian dolls. Overall, the field distribution exhibits a fractal-like structure.

The space-time distributions of the longitudinally polarized electric field of α-type STPs are shown in Fig. S2. Both the number of lobes and the number of singularities (including vortices and saddle points) increase with α. In the figure, vortices and saddle points are marked by ○ and ●, respectively, and are labeled as V and S followed by their indices. The longitudinal field varies smoothly around each singularity, transitioning from a maximum to zero and then to a minimum, indicating a continuous change of the field vector between longitudinal and transverse orientations. To illustrate this more clearly, Fig. S3 presents the local vector field distributions around vortex V1 and saddle point S1 for α = 4. As shown, the electric field vectors rotate around the vortex center, whereas around the saddle point the vectors exhibit opposite behaviors along two orthogonal directions: converging toward the saddle point in one direction while diverging away in the perpendicular direction. During propagation, the space-time field distribution and singularities of the STPs evolves continuously.

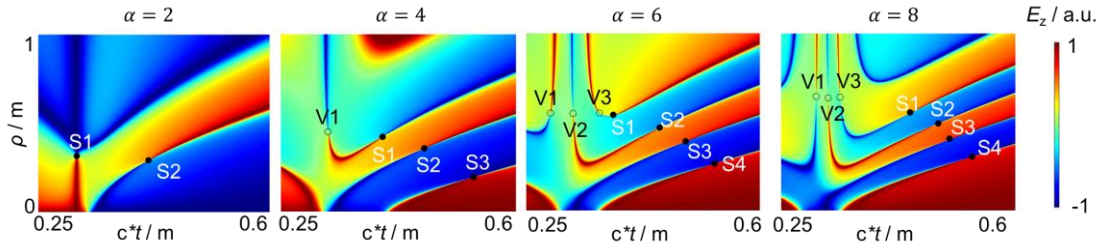


Fig. S2. Space-time distributions at *z*=0.32 m of the longitudinally polarized electric field of *α*-type STPs. In the figure, vortices and saddle points are marked by ○ and ●, respectively, and are labeled as V and S followed by their indices. Both the number of lobes and the number of singularities (including vortices and saddle points) increase with α. The longitudinal field varies smoothly around each singularity, transitioning from a maximum to zero and then to a minimum, indicating a continuous change of the field vector between longitudinal and transverse orientations.

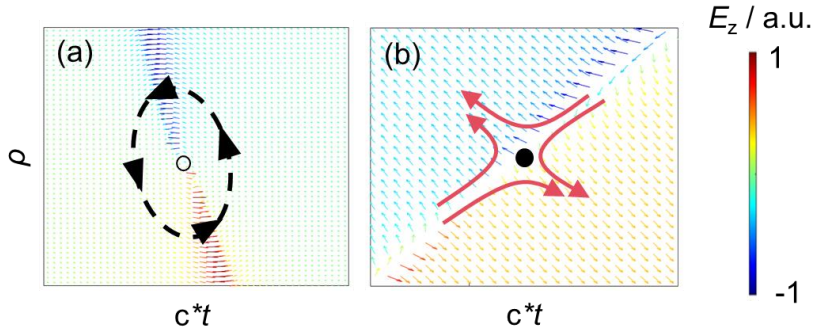


Fig. S3. Local vector field distributions around (a) vortex V1 and (b) saddle point S1 for *α* = 4. The electric field vectors rotate around the vortex center, whereas around the saddle point the vectors exhibit opposite behaviors along two orthogonal directions: converging toward the saddle point in one direction while diverging away in the perpendicular direction.

2. Spectral lobes of STPs.

The spectra of STPs exhibit multiple curved stripe patterns, and the number of spectral lobes increases with α. To examine this dependence, we analyzed the spectrum at z = 0.32 m and ρ = 0.6 m by taking the logarithm of the normalized field E_r. All local maxima exceeding –45 dB were counted as spectral lobes, with the total number of lobes minus one (the main lobe) giving the number of sidelobes. The resulting dependence of sidelobe number on α is shown in Fig. S4, calculated using Eq. (2) with parameters q_1=0.01m, q_2=50q_1, and $q_2 \to \infty$. As seen, no sidelobes are present for α = 1 (the toroidal pulse case); one sidelobe appears for α = 2; two sidelobes for α = 3 and 4; three sidelobes for α = 5 and 6; and four sidelobes for α = 7–9. The same sidelobe counts for different α arise from the thresholding criterion, since only maxima above –45 dB were considered. Because the spectra evolve gradually with α, the exact sidelobe count can vary with the choice of threshold. In practice, higher-precision counting of sidelobes has limited relevance, as the generation of STPs is accompanied by noise and distortions. For example, when a Vivaldi array with four rings of antenna elements was used, the measured spectrum showed more lobes than with three rings, but with noticeable splitting and irregularities that prevented accurate counting. Nevertheless, the observed spectral patterns exhibit similarity to the theoretical spectra for α = 7–9, and the representative case of α = 8 is used for comparison in the manuscript.

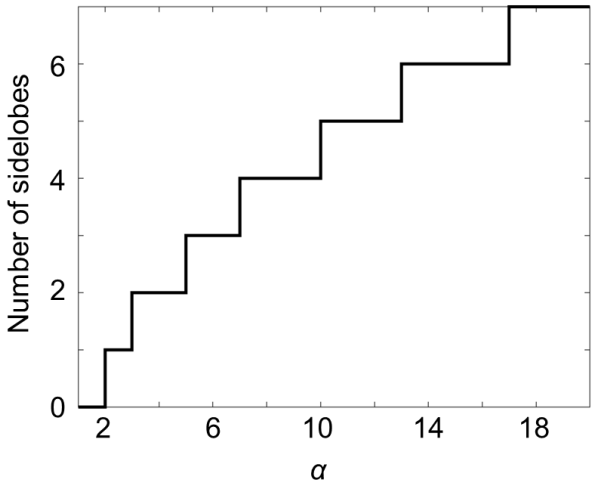


Fig. S4. Dependence of sidelobe number on *α*. All local maxima exceeding –45 dB are counted as spectral lobes, with the total number of lobes minus one (the main lobe) giving the number of sidelobes. The resulting dependence of sidelobe number on α is shown in Fig. S4, calculated using Eq. (2) with parameters q_1=0.01m, q_2=50q_1, and q_2 →∞. The analyzed spectrum is at z = 0.32 m and ρ = 0.6 m by taking the logarithm of the normalized field E_r. No sidelobes are present for α = 1 (the toroidal pulse case); one sidelobe appears for α = 2; two sidelobes for α = 3 and 4; three sidelobes for α = 5 and 6; and four sidelobes for α = 7–9.

3. Vivaldi antenna and array.

The α-type STPs are generated using a concentric-ring Vivaldi antenna array. The employed Vivaldi antenna exhibits ultrawideband performance, covering approximately 2–10 GHz, as shown in Fig. S5, thereby satisfying the broad spectral requirements of STPs.

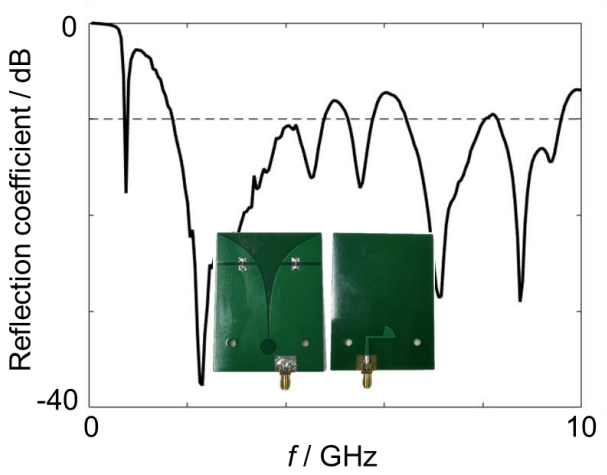


Fig. S5. Measured reflection coefficient of the Vivaldi antenna used for generating *α*-type STPs. The antenna exhibits ultrawideband characteristics spanning 2–10 GHz. The dashed line indicates the –10 dB level: within the 2–10 GHz range, most frequency points have reflection coefficients below –10 dB, while a few exceed –10 dB but remain below –6 dB. The insets show front and back views of the Vivaldi antenna.

In the concentric-ring Vivaldi antenna array, all antenna elements are radially polarized to match the transverse polarization of STPs. The elements are placed every 30° along the azimuth, with 12 elements per ring. Arrays with 1, 2, 3, and 4 rings are used to generate *α*-type STPs with α = 2, 4, 6, and 8, respectively. A photograph of the Vivaldi antenna array with four rings is shown in Fig. S6.



Fig. S6. Photograph of the Vivaldi antenna array with four concentric rings. Each Vivaldi element is radially polarized to match the transverse polarization of STPs. The elements are spaced every 30° along the azimuth, with 12 per ring.

4. Coaxial horn antenna

The toroidal pulse generator used in this paper is a broadband, radially polarized coaxial horn antenna [14], purposely designed to produce toroidal pulses with parameters q_1=0.01m and q_2=50q_1. The structure and parameters of the coaxial horn antenna used to generate the toroidal pulses are shown in Fig. S7. The antenna is formed by flaring the inner and outer conductors of a coaxial waveguide outward into a horn shape and fed from the base through a coaxial connector supporting the rotationally symmetric transverse electric and magnetic (TEM) mode [14]. The distance between the coaxial horn and the metasurface is 0.5 m.

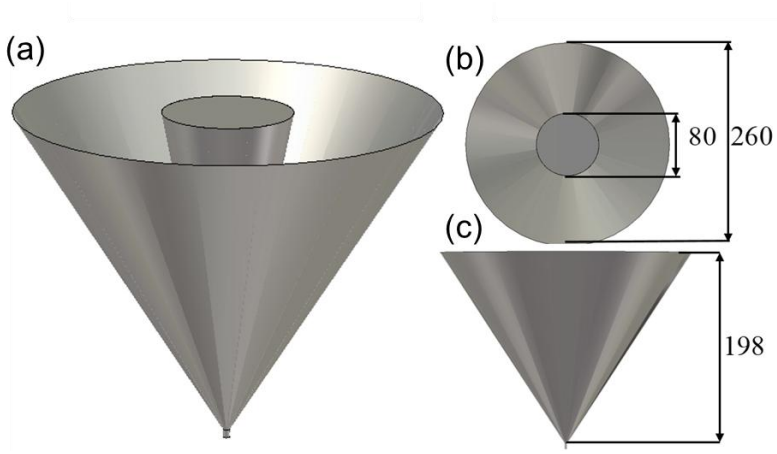


Fig. S7. Structure of the coaxial horn antenna used to generate TM toroidal pulses (dimensions in mm): (a) Overall view of the horn antenna; (b) top view; (c) side view. The antenna is formed by flaring the inner and outer conductors of a coaxial waveguide

outward into a horn shape and fed from the base through a coaxial connector supporting the rotationally symmetric TEM mode.

In a coaxial waveguide, the magnetic field encircles the inner conductor, corresponding to the azimuthally polarized component of the TM toroidal pulses, while the electric field is radially polarized, corresponding to its radial component, as illustrated in Fig. S8. According to Gauss's law, the radially polarized electric field component cannot exist in isolation; it necessarily induces a longitudinally polarized electric field given by

$$E_z(\rho, z) = -\int_{z_0}^{z} \frac{\partial E_\rho(\rho, z')}{\partial \rho} dz' \quad \text{(S1)},$$

where z_0 is chosen as a reference point at which the field vanishes. This coupling of field components gives rise to the formation of toroidal pulses.

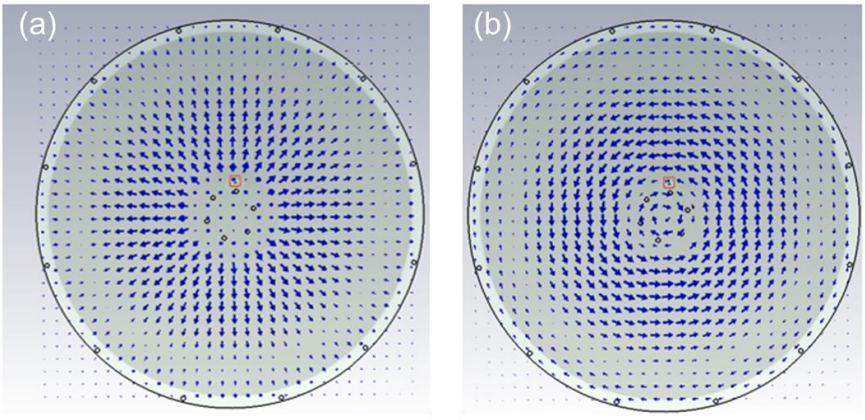


Fig. S8. Transverse electromagnetic field distributions in the coaxial horn antenna: (a) Radially polarized electric field; (b) azimuthally polarized magnetic field.

5. Metasurfaces with spatially distributed frequency-selective functionality

The metasurfaces designed in this work incorporate spatially distributed frequency-selective functionality. The surface comprises 22 concentric rings of frequency-selective elements, positioned at radii of 25 mm, 33 mm, 42 mm, 50 mm, 60 mm, 70 mm, 80 mm, 90 mm, 100 mm, 110 mm, 122.5 mm, 136.5 mm, 150 mm, 165 mm, 182 mm, 200 mm, 225 mm, 250 mm, 274 mm, 300 mm, 350 mm, and 400 mm from the array center. Elements in rings 1–4 are arranged at 20° intervals, with 18 elements per ring; elements in rings 5–22 are also spaced at 20° intervals, with 36 elements per ring.

The frequency-selective surface (FSS) elements were designed using the topology optimization module in COMSOL. The incident wave was set as x-polarized, and the initial structure consisted of a dielectric substrate clad with metal on the upper surface. The dielectric substrate had a thickness of 2 mm and was made of F4B with a relative permittivity of 2.65.

The objective function was defined as $\min f = -w_1 S_{11x}\big|_{f_1} + w_2 S_{11x}\big|_{f_2} - w_3 S_{11x}\big|_{f_3}$, (S2)

where S_{11x} denotes the S-parameter for x-polarized incidence, f_1 and f_3 are frequencies to be rejected, f_2 is the desired pass frequency, w_1, w_2 and w_3 are the corresponding weighting factors. Since frequency-domain simulations were used, only three frequency points were selected in the objective function to reduce computational time.

Taking the optimization of the 22nd ring element as an example, the design goal was to transmit an electromagnetic wave at 2 GHz. The initial structure's side length l was set close to one-quarter wavelength, at 37.5 mm. To accelerate convergence, a split-ring

resonator (SRR) structure was used as the initial design. Since it serves only as a starting point, the SRR parameters were set arbitrarily here: outer radius r_1=10.5 mm, inner radius r_2=7 mm, and gap width s=2.1 mm. The target frequencies were f_1=1.5GHz, f_2=2GHz, f_3=2.5GHz, with w_1=1, w_2=1, w_3=1.

During optimization, the objective function value versus iteration number is shown in Fig. S9. The value decreases rapidly within the first 50 iterations and then gradually stabilizes. Convergence was reached at 153 iterations when the preset tolerance was met, ending the simulation. The final optimized S-parameters were $S_{11x}(f_1)$ = -0.36 dB, $S_{11x}(f_2)$ = -30 dB, $S_{11x}(f_3)$ = -0.16 dB.

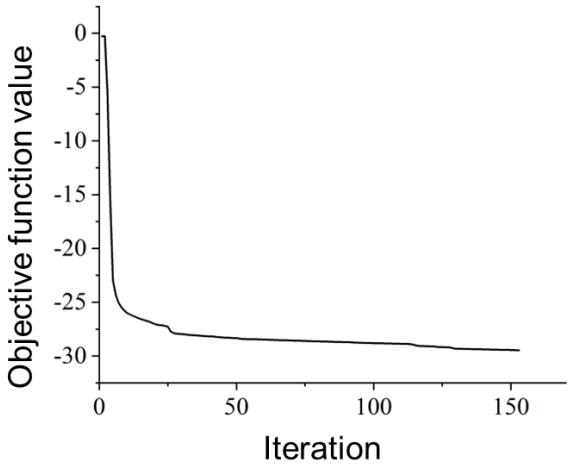


Fig. S9. Variation of the objective function value for the 22nd ring element. The value decreases rapidly during the first 50 iterations and then gradually stabilizes.

The distribution of the optimized variables is shown in Fig. S10, where a value of 1 indicates metal and 0 indicates air. The extracted structure is obtained by applying a threshold to the optimized distribution. When convergence is satisfactory, the choice of threshold has little effect on the result; here, a threshold of 0.3 was used. The resulting

structure is shown in Fig. S11.

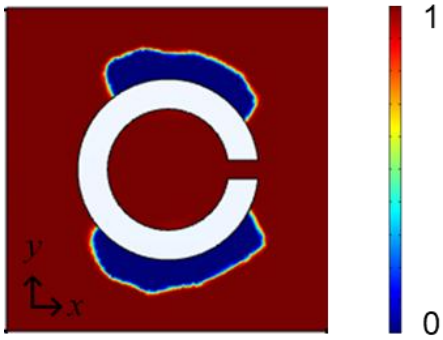


Fig. S10. Distribution of the optimized variables for the 22nd ring element. The white regions correspond to the initial split-ring resonator structure, with a value of 1 indicating metal and 0 indicating air.

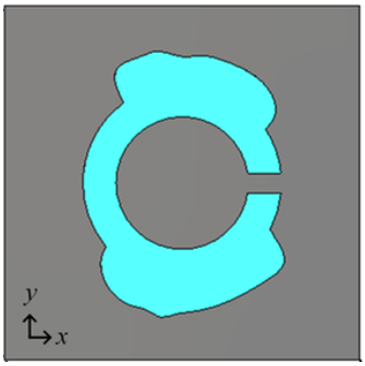


Fig. S11. Topology-optimized structure of the 22nd ring element. Gray and aquamarine regions represent metal and the dielectric substrate exposed at locations where metal has been etched, respectively.

To verify that the topology-optimized structure achieves the desired performance, the design in Fig. S11 was simulated. The S-parameters are presented in Fig. S12, showing $S_{11x}(f_1)$ = -0.32 dB, $S_{11x}(f_2)$ = -47.3 dB, $S_{11x}(f_3)$ = -0.17 dB, which agree well with the optimization results.

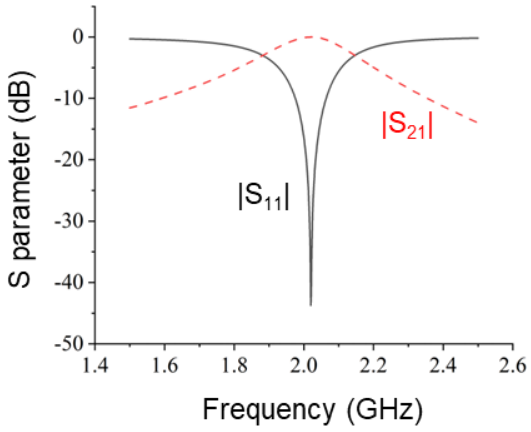


Fig. S12. S-parameters of the optimized structure for the 22nd ring element. The passband location agrees with the design targets.

Using the method described above, a metasurface comprising 22 concentric rings of unit cells was ultimately designed, as shown in Fig. S13, with the transmission coefficients of the optimized unit cells presented in Fig. S14. The metasurface is specifically designed to manipulate the transverse polarization component, with each concentric ring exhibiting distinct transmission frequencies. From the innermost to the outermost rings, the unit cell dimensions gradually increase, causing the central resonance frequency of the elementary mode to decrease from approximately 10 GHz to around 2 GHz. The elementary-mode transmission bands of neighboring unit cells partially overlap, and the higher-order mode transmission frequencies of the outer-ring unit cells overlap with the elementary-mode transmission frequencies of the inner-ring unit cells. Consequently, the transmission spectra of the different unit cells undergo diffraction and interference after passing through the metasurface, producing the curved stripe pattern required for generating STPs.

Furthermore, because each ring transmits only a portion of the transverse polarization

frequencies, the transverse component of the toroidal pulse is significantly reduced after transmission. As shown in Fig. 5 of the manuscript, the ratio of longitudinally to transversely polarized field components increases substantially after transmission compared to the original toroidal pulse.

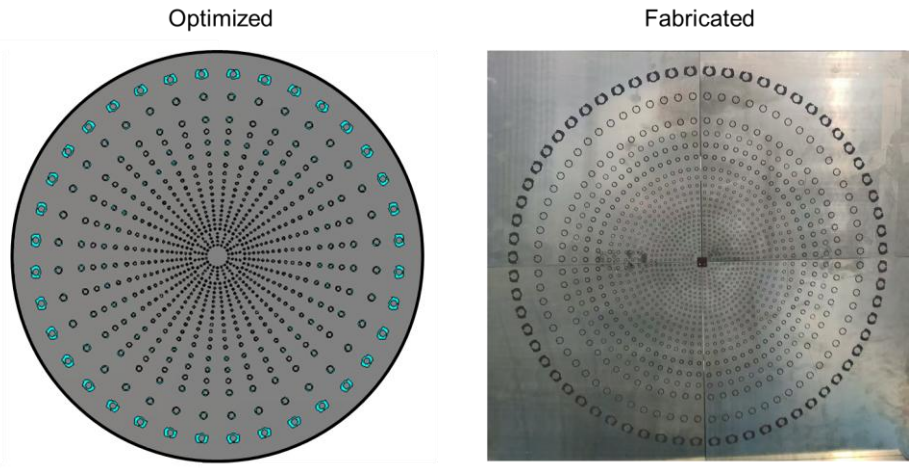


Fig. S13. Metasurface with spatially distributed frequency-selective functionality. The surface consists of 22 concentric rings of frequency-selective elements. Elements in rings 1–4 are arranged at 20° intervals, with 18 elements per ring; elements in rings 5–22 are also spaced at 20° intervals, with 36 elements per ring. The fabricated metasurface is assembled from four separately fabricated dielectric panels, each occupying one quadrant.

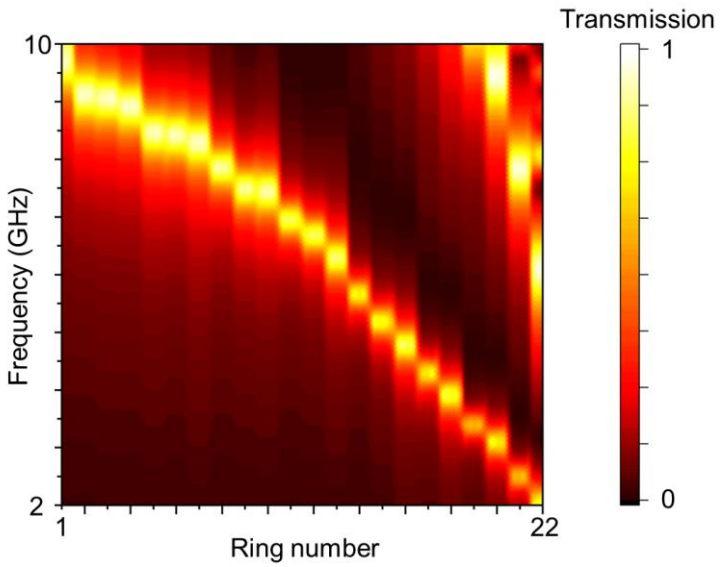


Fig. S14. Transmission coefficients of the metasurface unit cells for each ring. From the innermost to the outermost rings, the central resonance frequency of the elementary mode decreases from approximately 10 GHz to around 2 GHz. The elementary-mode transmission bands of several adjacent unit cells partially overlap, and the higher-order mode transmission frequencies of the outer-ring unit cells overlap with the elementary-mode transmission frequencies of the inner-ring unit cells.

6. Excitation signal

(1) Vivaldi antenna:

Considering that the aperture field of the antenna effectively acts as a differentiator, the excitation signal was designed as the temporal integral of the corresponding pulses to ensure that the pulses radiated by the antenna exhibit a temporal (and equivalently spectral) profile similar to that of theoretical pulses. In this design, the feeding voltage waveform corresponds to the radial integral of the transversely polarized component of target pulses, as illustrated in Fig. S15.

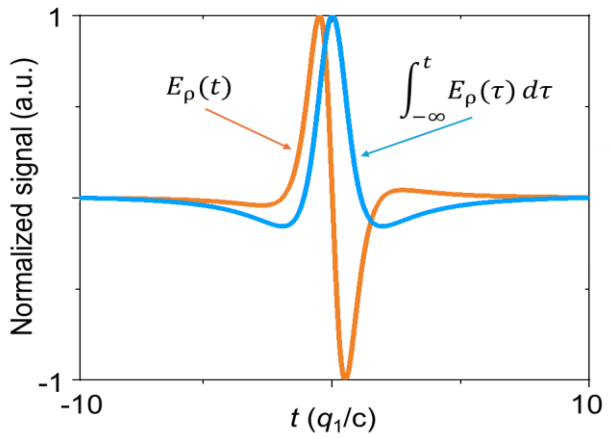


Fig. S15. Excitation signal. The feeding voltage waveform corresponds to the radial integral of the transversely polarized component of target pulses.

(2) Coaxial horn antenna:

The input signal $g_f(t)$ can be determined once the spatial response $h(\omega,\rho)$ of the generator has been obtained through measurement. To better match the target spatiotemporal field, the signal at a specific location ρ_1 of the target field is selected as the reference signal $y_t(\omega,\rho_1)$. The input signal that ensures the field at ρ_1 coincides with the theoretical field can then be calculated as $g_f(\omega)=y_t(\omega,\rho_1)/h(\omega,\rho_1)$, and the corresponding time-domain signal is given by $g_f(t)$. In practice, the excitation signal can be optimized by iteratively adjusting the chosen reference location ρ_1, thereby obtaining an input signal that produces a three-dimensional field distribution that best matches the desired theoretical field.

7. Experimental setup and measurement method

The electromagnetic fields of the generated STPs were measured in a microwave anechoic chamber using a three-dimensional scanning rail system, as shown in Fig. S16. For α-type STPs, the receiving antenna was the Vivaldi array connected through a

divider system; for *k*-type pulses, the receiving antenna was the toroidal pulse generator, i.e., a coaxial horn antenna. In both cases, standard rectangular horn probes and monopole probes were used as transmitting antennas to measure the transverse and longitudinal polarization components, respectively. The probes were mounted on the scanning rails, allowing computer-controlled three-dimensional movement. For *k*-type measurements, the metasurface and coaxial horn were aligned coaxially with a fixed separation of 0.5 m, while the probe-to-device distance was adjustable to sample fields at different positions. For α-type measurements, the probes could also scan radially across the Vivaldi array to map spectral distributions. A vector network analyzer was used to record the S_{21} parameter, providing the magnitude and phase of the fields at different spatial locations.

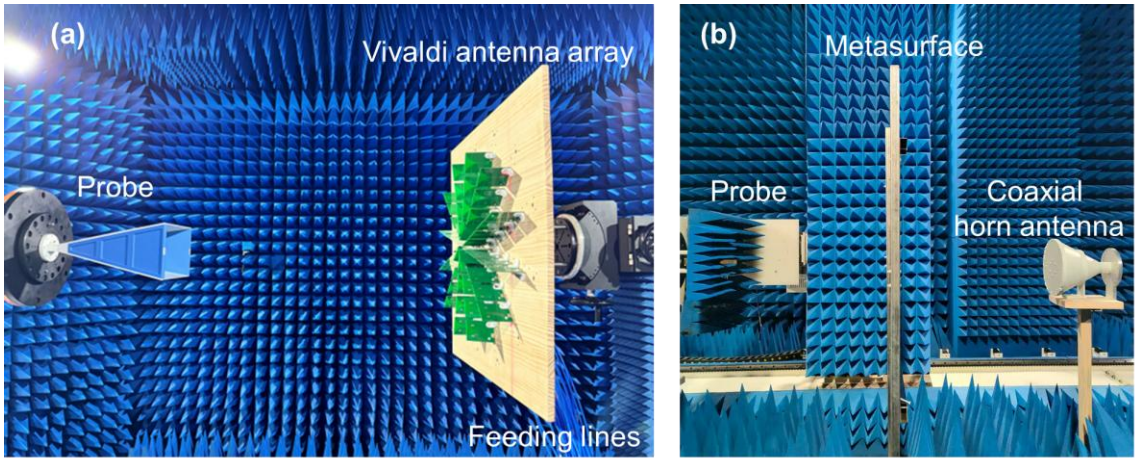


Fig. S16. Experimental measurement setups for (a) *α*-type and (b) *k*-type STPs. In (a), the receiving antenna was the Vivaldi array connected through a divider system; in (b), it was the toroidal pulse generator (coaxial horn). In both cases, standard rectangular horn probes and monopole probes were used as transmitting antennas to measure the transverse and longitudinal polarization components, respectively. The

probes were mounted on scanning rails for three-dimensional positioning. In (a), the probe-to-array distance was adjustable; in (b), the metasurface and coaxial horn were coaxially aligned with a fixed 0.5 m separation, while the probe-to-device distance was adjustable.

Fig. S17 compares the longitudinally polarized spectral distributions of the theoretical and experimentally generated α-type STPs. The theoretical results were calculated using Eq. (2) with parameters q_1=0.01m, q_2=50q_1, and $q_2 \to \infty$. Similar to the transversely polarized cases in Fig. 2, the measured results exhibit stripe patterns characteristic of STPs but differ slightly from the theoretical case. Nevertheless, both the theoretical and experimental spectra feature multiple curved stripe patterns. In particular, the transverse component vanishes along the propagation axis (ρ=0), where the longitudinal component reaches its maximum. With increasing α, the number of spectral lobes in the theoretical STPs increases; correspondingly, as the number of Vivaldi antenna rings in the array increases, the measured spectra also exhibit more lobes. The spectra generated by arrays of 1, 2, 3, and 4 rings of Vivaldi antenna elements correspond to the theoretical spectra for α = 2, 4, 6, and 8, respectively.

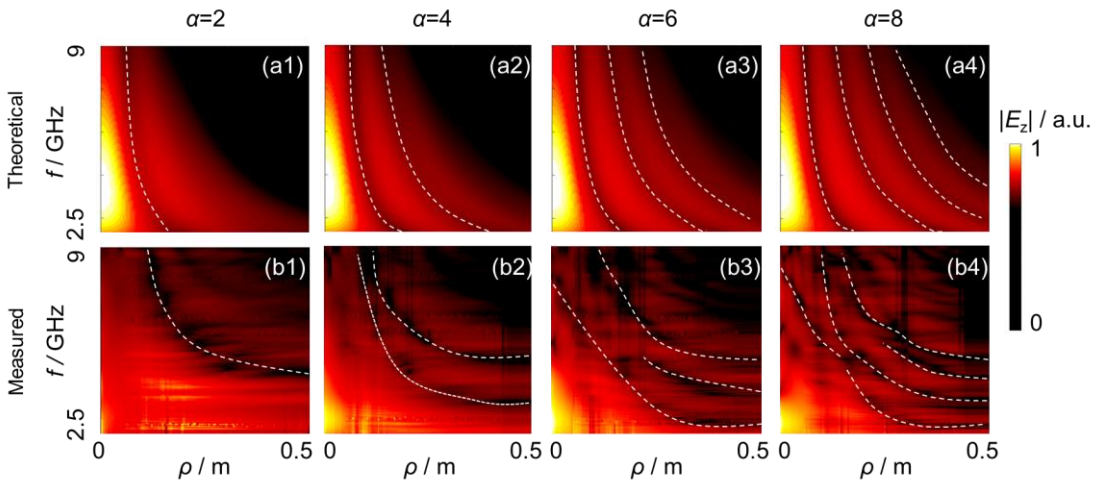


Fig. S17. Longitudinally polarized spectral distributions of *α*-type STPs. (a1–a4) and (b1–b4) present the theoretical and measured spectra of the longitudinal polarization components, respectively, which reach their maximum intensity on the propagation axis. The white dashed lines serve as visual guides to delineate the boundaries between different lobes. All results correspond to z=0.32 m. The theoretical spectra in the first to fourth columns are obtained by Fourier transforming the STPs calculated with parameters q_1=0.01m, q_2=50q_1, for α = 2, 4, 6, and 8, respectively. The measured spectra in the first to fourth columns correspond to arrays composed of 1, 2, 3, and 4 rings of Vivaldi antenna elements, respectively. Both theoretical and generated STPs exhibit multiple curved stripe patterns in their spectra. Both theoretical and generated pulses exhibit multiple curved stripe patterns. As α increases, the theoretical spectra develop additional lobes; correspondingly, increasing the number of array rings leads to more lobes in the measured spectra. The measured spectra from arrays with 1 to 4 rings match with the theoretical spectra of α = 2, 4, 6, and 8, respectively.

8. Method for reconstructing the time-domain field from measured spectra

The simulated time-domain fields were obtained using the time-domain solver by directly exciting the coaxial horn antenna with a voltage waveform applied between its inner and outer conductors, corresponding to the radial integral of the transversely polarized component of the toroidal pulses.

Experimentally, the time-domain fields were reconstructed from frequency-domain measurements. The spatial amplitude and phase distributions were obtained using the methods described in Section 7. The time-domain response was then computed via inverse Fourier transform, providing direct evidence of the generation of STPs.

Fig. S18 reveals that the spectra of both theoretical and generated pulses display multiple curved stripe patterns; notably, the transverse component vanishes on the propagation axis, where the longitudinal component reaches its maximum. Compared with the spectral distributions of α-type STPs in Fig. 2, the k-type pulses display more spectral sidelobes, resembling those of α-type pulses with large α.

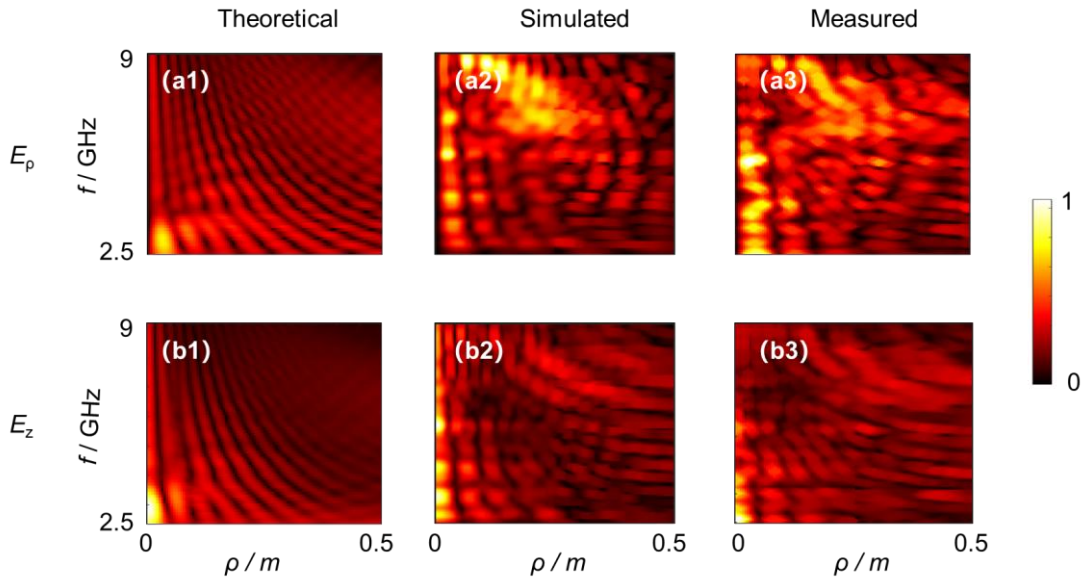


Fig. S18. Spectral distributions of *k*-type STPs. (a1–a3) Theoretical, simulated, and measured spectra of the transverse polarization components, showing zero intensity along the propagation axis. All results correspond to a propagation distance of 0.5 m from the aperture. The theoretical results are derived from ideal STPs truncated at a 0.5 m aperture radius, while the simulated and measured results are generated by toroidal pulses emitted from a coaxial horn antenna and transmitted through a metasurface with a 0.5 m aperture radius. (b1–b3) Theoretical, simulated, and measured spectra of the longitudinal polarization components, with maximum intensity at the propagation axis. Both theoretical and generated STPs exhibit multiple curved stripe patterns in their spectra.

After system calibration, the amplitude- and phase-frequency responses, $E_{\mathrm{abs}}(f,\rho,z)$ and $E_{\mathrm{arg}}(f,\rho,z)$, were used to construct the complex spectral response:

$$F_{\mathrm{meas}}(f,\rho,z) = E_{\mathrm{abs}}(f,\rho,z) * e^{i*E_{\mathrm{arg}}(f,\rho,z)}, \tag{S3}$$

$$T_{\mathrm{meas}}(t,\rho,z) = \frac{1}{2\pi}\int_{-\infty}^{+\infty} F_{\mathrm{meas}}(\omega,\rho,z)\, e^{i\omega t} d\omega. \tag{S4}$$

The coaxial horn antenna was fed with the signal $g_{\mathrm{f}}(t)$. The antenna's capacitive loading ensures that the radiated waveform corresponds to the time derivative of the driving signal, closely matching the temporal profile of the free-space toroidal pulse at z=0. The resulting spatiotemporal field distribution $E_{\mathrm{st}}(t,\rho,z)$ generated by the setup in Fig. 1 can be expressed as

$$E_{\mathrm{st}}(t,\rho,z) = T_{\mathrm{meas}}(t,\rho,z) \otimes g_{\mathrm{f}}(t) \tag{S5}$$

where $\otimes$ denotes convolution.

9. Calculation method for the propagation characteristics of theoretical STPs with finite apertures.

Ideal STPs possess a large transverse extent and a broad frequency spectrum [32–35], conditions that are challenging to realize in practical applications. To enable comparison with experimentally generated pulses of finite aperture and spectrum, both the transverse size and frequency range of the theoretical pulses were truncated. This allows examination of whether the theoretical features predicted in [32–35]—including skyrmion textures, vortex street topology, nondiffracting propagation, superoscillation behavior, and strong longitudinal polarization—can still be preserved under these constraints.

For *k*-type STPs, the STPs are generated using a coaxial horn antenna combined with a metasurface possessing spatially distributed frequency-selective properties. The coaxial horn antenna operates effectively over the 2–9 GHz range, and the designed metasurfaces are matched to this band, with an aperture radius of approximately 0.5 m.

Accordingly, the fields of the theoretical STPs were first subjected to a spatiotemporal Fourier transform. At the plane z=0, the aperture size and frequency range were truncated to match the above limits, and an inverse Fourier transform was then applied to obtain the corresponding finite-aperture, finite-spectrum source at z=0. The propagation characteristics of these pulses beyond the source plane were subsequently calculated using the aperture field method.

The aperture field method determines the radiated field from equivalent electric and magnetic current sources $\boldsymbol{J}$ and $\boldsymbol{J}^{\mathrm{m}}$ defined on the aperture plane. For the transversely polarized components of the truncated field, the equivalent sources are given by

$$\boldsymbol{J} = \left(-H_y,\ H_x,\ 0\right),\ \ \boldsymbol{J}^{\mathrm{m}} = \left(E_y,\ -E_x,\ 0\right). \tag{S6}$$

The fields radiated by the electric current source $\boldsymbol{J}$ are

$$\boldsymbol{E}^{\mathrm{e}} = -j\omega\mu\boldsymbol{A} + \frac{1}{j\omega\varepsilon}\nabla(\nabla\cdot\boldsymbol{A}), \tag{S7}$$

$$\boldsymbol{H}^{\mathrm{e}} = \nabla\cdot\boldsymbol{A}, \tag{S8}$$

$$\boldsymbol{A} = \frac{1}{4\pi}\int \boldsymbol{J}\psi dv', \tag{S9}$$

where $\psi = e^{-jkR}/R$, k is the wavenumber, R is the distance between the source and observation points, ω is the angular frequency, μ is the permeability, and ε is the permittivity. The prime "′" denotes integration over the source coordinates.

Similarly, the fields radiated by the magnetic current source $\boldsymbol{J}^{\mathrm{m}}$ are

$$\boldsymbol{H}^{\mathrm{m}} = -j\omega\varepsilon\boldsymbol{F} + \frac{1}{j\omega\mu}\nabla(\nabla\cdot\boldsymbol{F}), \tag{S10}$$

$$\boldsymbol{E}^{\mathrm{m}} = -\nabla\cdot\boldsymbol{F}, \tag{S11}$$

$$\boldsymbol{F} = \frac{1}{4\pi}\int \boldsymbol{J}^{\mathrm{m}}\psi dv' . \tag{S12}$$

The total fields after propagation are then given $\boldsymbol{E} = \boldsymbol{E}^{\mathrm{e}} + \boldsymbol{E}^{\mathrm{m}}, \boldsymbol{H} = \boldsymbol{H}^{\mathrm{e}} + \boldsymbol{H}^{\mathrm{m}}$.

10. Discussion on skyrmion textures in STPs

Near adjacent vortex rings in vortex-street patterns, oppositely oriented skyrmions are present, as shown in Figs. S19(a1–b3), consistent with theoretical predictions in [32]. To quantitatively evaluate the electric field vector distribution, the skyrmion number of the textures depicted in Figs. S19(a1–b3) was calculated.

The skyrmion number is defined as the spatial integral of the topological charge density and can be calculated using:

$$N_{\mathrm{sk}}(\boldsymbol{\rho}) = \frac{1}{4\pi}\iint \boldsymbol{m}(\boldsymbol{\rho})\cdot\left[\frac{\partial \boldsymbol{m}(\boldsymbol{\rho})}{\partial x}\times\frac{\partial \boldsymbol{m}(\boldsymbol{\rho})}{\partial y}\right]\mathrm{d}x\mathrm{d}y \tag{S13}$$

where $\boldsymbol{m}(\boldsymbol{\rho}) = \boldsymbol{E}(\boldsymbol{\rho})/|\boldsymbol{E}(\boldsymbol{\rho})|$ is the unit vector used to construct the skyrmions, and $\boldsymbol{E}(\boldsymbol{\rho})$ denotes the electric field vector at each position. The size of the calculation domain is chosen according to the dimensions of the skyrmions, with the boundary set at the location where the longitudinal electric field appears for the second time. Applying Eq. (S13) yields a skyrmion number of approximately ±1, as shown in Fig. S19, confirming the presence of skyrmionic textures in the generated electromagnetic toroidal pulses.

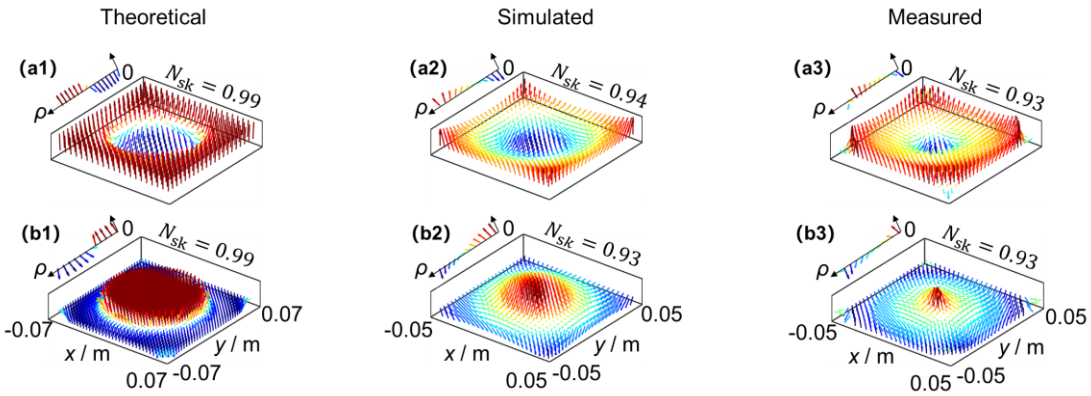


Fig. S19. Skyrmion textures in the generated STPs. Oppositely oriented skyrmion textures appear near adjacent vortex rings. The skyrmion textures on the two sides of the vortex-ring center are shown in (a1–a3) and (b1–b3), respectively. The calculated skyrmion numbers, denoted as N_{sk} in this figure, are close to ±1, confirming well-defined skyrmion structures.

The vector structure of skyrmions can also be visualized using the directional coverage on a unit sphere. Each vector in a two-dimensional plane is normalized and mapped from the origin onto the unit sphere based on its orientation. Complete coverage of the sphere by vectors within a target area provides an intuitive indication of skyrmion presence. Fig. S20 shows the directional sphere coverage for theoretical, simulated, and measured STPs. In all cases, the vectors span the entire sphere, visually confirming the existence of skyrmions.

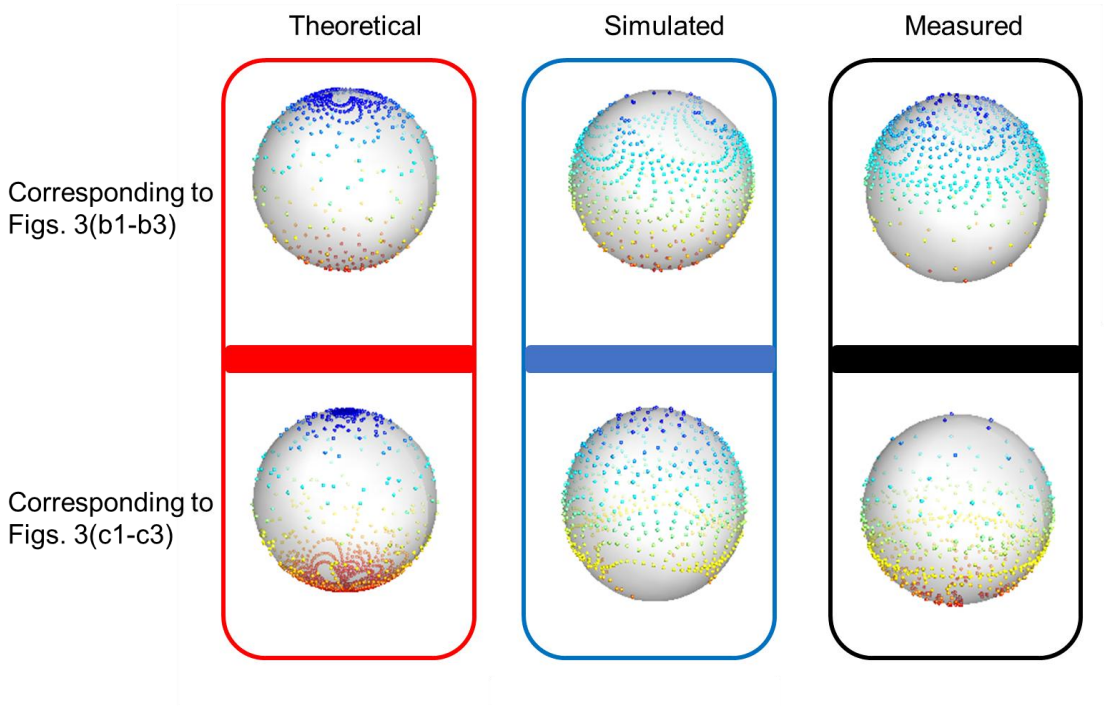


Fig. S20. Sphere of directions for theoretical, simulated, and measured STPs. The vectors fully cover the surface of the sphere, visually confirming the presence of skyrmions.

For *k*-type STPs, as theoretically predicted in [32], the electric field vectors of the STPs form multiple concentric nested target skyrmion textures over a larger transverse cross-section, as illustrated in Fig. S21. Fig. S19 corresponds to the central region of Fig. S21.

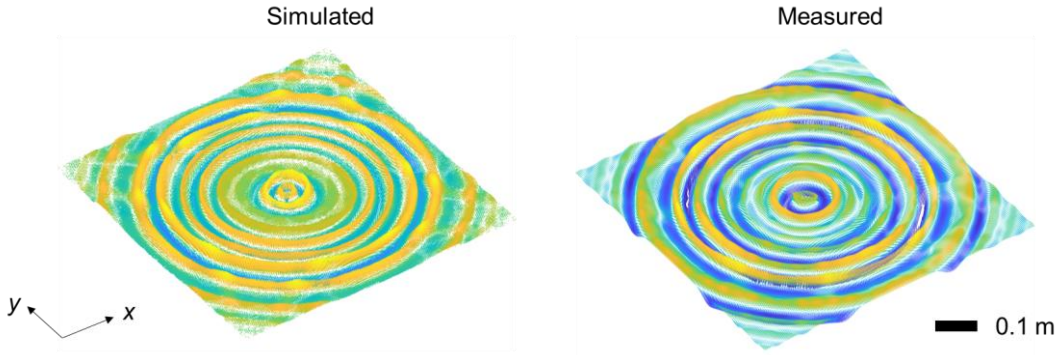


Fig. S21. Electric field distributions over a large-aperture region. Both simulated

and measured fields exhibit concentric target skyrmion textures.

11. Discussion on the superoscillation of STPs

In addition to the transversely polarized component shown in Fig. 3, space–time superoscillations are also observed in the longitudinally polarized component of the STPs. Fig. S22 shows the longitudinal electric fields of the STPs at z=0.32m, illustrating space-time superoscillation phenomena. In both theoretical and measured cases, the spectral components of the STPs below 8 GHz were selected, and the corresponding space–time electric fields were obtained via inverse Fourier transform of the truncated spectra. For the longitudinal component, spatial superoscillations are absent at α=2, 4, and 6, but emerge on the propagation axis (ρ=0) at α=8 in both theory and experiment. These results indicate that for smaller α, neither the transverse nor the longitudinal components exhibit spatial superoscillations, whereas at larger α, spatial superoscillations appear consistently.

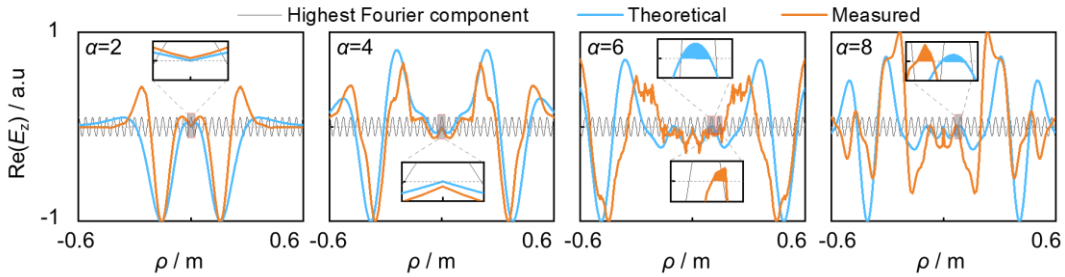


Fig. S22. Longitudinally polarized spatial superoscillation of α-type STPs. Both theoretical and measured STPs share the same highest frequency of 8 GHz, and their field-line evolution trends agree well for α=2,4,6, and 8. The gray curve in the figure represents an 8-GHz sinusoidal wave with a wavelength of 3.75 cm. The horizontal axis

spans 32 wavelengths at 8 GHz, corresponding to a total length of 1.2 m. For the longitudinal component, no clear superoscillation phenomenon appears at α=2,4, or 6, while at α=8, superoscillations occur on the propagation axis (ρ=0) in both theory and experiment.

The time-domain signals of the transversely polarized fields for α=6 and longitudinally polarized fields for α=8 at the spatial superoscillation locations are examined, as shown in Figs. S23(a) and (b). The results indicate that temporal superoscillations are indeed present at the locations of spatial superoscillations for both the transversely and longitudinally polarized fields, thereby confirming the occurrence of space–time superoscillations. Although device imperfections lead to slight mismatches between theory and experiment in the exact positions and times at which these effects appear, Figs. S22 and S23 provides clear experimental evidence of the space–time superoscillation phenomenon.

The longitudinal field distribution of *k*-type STPs is shown Figs. S24(a1–a3), showing concentration along the propagation axis. Interestingly, superoscillation phenomena are observed near positions where the longitudinal field changes sign along the axis, as shown in Fig. S24(b). In the experiment, the maximum measured frequency was 9 GHz; for comparison, the theoretical and simulated spectra were truncated at this frequency, and the corresponding theoretical and simulated results were obtained accordingly. Fig. S24(b) reveals that near ρ=0, the theoretical, simulated, and measured longitudinal electric fields exhibit spatial oscillations at frequencies higher than the highest Fourier component (corresponding to 9 GHz), confirming superoscillation

behavior. Unlike conventional superoscillations confined to tightly focused optical spots, the nondiffraction of STPs allows their superoscillation features to persist over extended propagation distances.

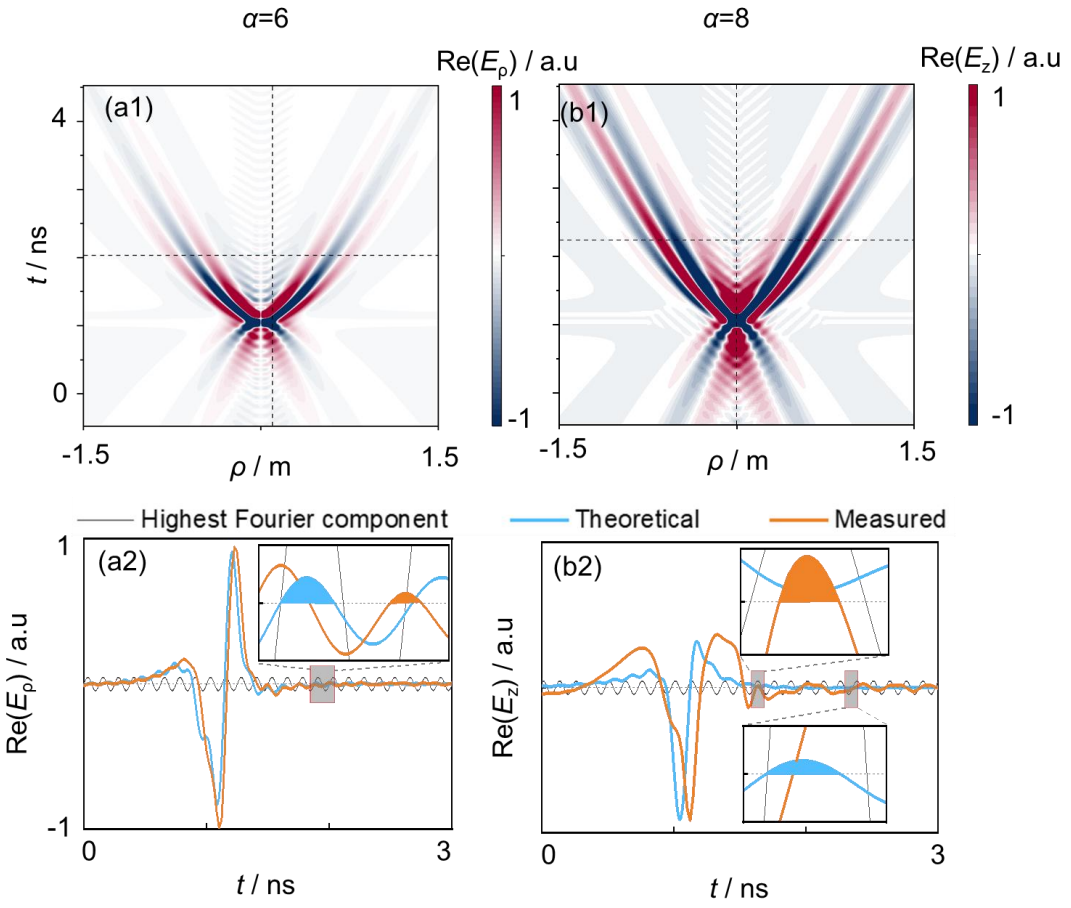


Fig. S23. Spatiotemporal superoscillation of α-type STPs. The time-domain signals of the transversely polarized fields for α=6 and longitudinally polarized fields for α=8 at the superoscillation locations are examined, as shown in (a1-a2) and (b1-b2), respectively. In the two-dimensional spatiotemporal field distribution, many pronounced side lobes can be observed near ρ=0; their spatial and temporal periods are both much smaller than those of the main lobes. This leads to spatial and temporal superoscillations, as indicated by the dashed lines in the figure. The intersection of these dashed lines corresponds to the occurrence of spatiotemporal superoscillation. The

results in the enlarged inset figures indicate that temporal superoscillations are indeed present at the locations of spatial superoscillations for both the transversely and longitudinally polarized fields, thereby confirming the occurrence of space–time superoscillations.

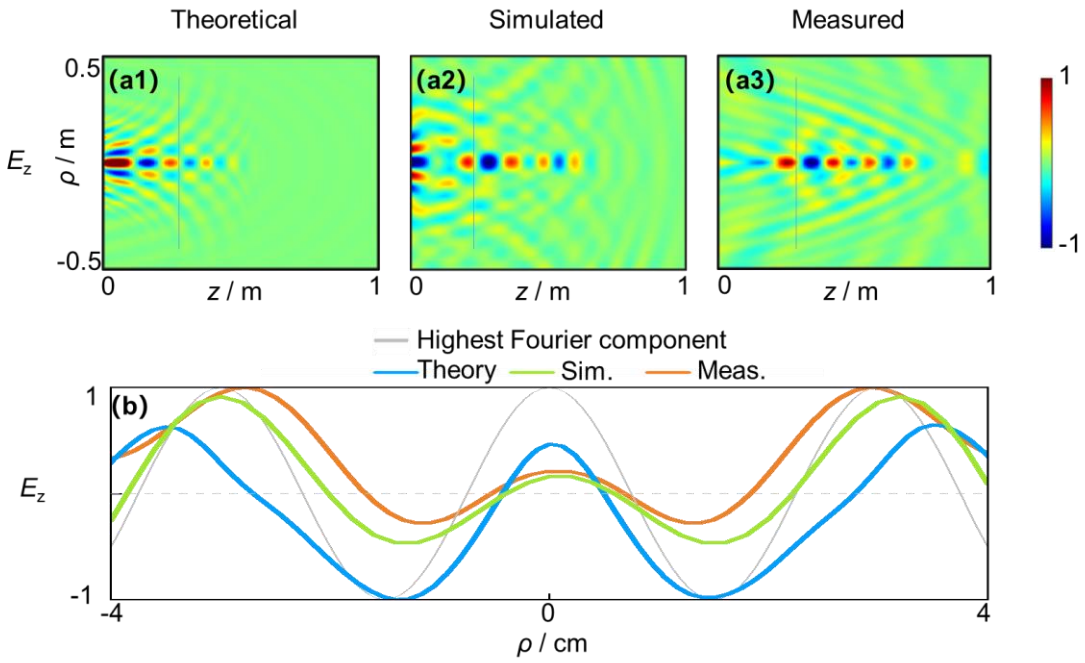


Fig. S24. Superoscillation of the generated STPs. (a1–a3) Distribution of the longitudinal field component of STPs. Near positions along the propagation axis where the longitudinal field changes sign, superoscillation phenomena are observed. For example, the fields along the gray lines in (a1–a3) are shown in (b). Near ρ=0, the theoretical, simulated, and measured longitudinal electric fields exhibit spatial oscillations smaller than the wavelength of the highest Fourier component (9 GHz).